



[www.sciencemag.org/content/343/6166/58/suppl/DC1](http://www.sciencemag.org/content/343/6166/58/suppl/DC1)

## Supplementary Materials for

### First-Photon Imaging

Ahmed Kirmani,\* Dheera Venkatraman, Dongeek Shin, Andrea Colaço, Franco N. C. Wong, Jeffrey H. Shapiro, Vivek K Goyal\*

\*Corresponding author. E-mail: akirmani@mit.edu (A.K.); vgoyal@ieee.org (V.K.G.)

Originally published 28 November 2013 on *Science Express*  
DOI: 10.1126/science.1246775

#### This PDF file includes:

Materials and Methods  
Supplementary Text  
Figs. S1 to S14  
Table S1  
References

#### Other Supplementary Material for this manuscript includes the following: available at [www.sciencemag.org/content/343/6166/58/suppl/DC1](http://www.sciencemag.org/content/343/6166/58/suppl/DC1)

Movies S1 and S2

**Correction (3 January 2014):** The previous supplementary materials file had old versions of Figs. S2 to S5. This version contains the correct, final figures, corrects two typographical errors associated with the old figures, and provides the correct e-mail address for V.K.G.

## Materials and Methods

### Equipment details:

The active illumination source was a 640-nm-wavelength pulsed laser diode that emitted pulses with  $T_p = 226$  ps RMS duration at a 10 MHz repetition rate and 0.6 mW average power. An incandescent lamp illuminated the detector to create background noise from extraneous photon detections. A two-axis scanning galvo (maximum scan angle  $\pm 20^\circ$ ) was used to raster scan a room-scale scene consisting of life-size objects. The laser spot size at 2 m distance was measured to be 1.5 mm. Prior to detection, the light was filtered using a free-space interference filter with 2 nm bandwidth centered at 640 nm wavelength whose peak transmission was 49%. The Geiger-mode APD was a Micro Photon Devices PDM series detector with  $100 \mu\text{m} \times 100 \mu\text{m}$  active area, 35% quantum efficiency, less than 50 ps timing jitter, and less than  $2 \times 10^4$  dark counts per second. The photon detection events were time stamped relative to the laser pulse with 8 ps resolution using a PicoQuant HydraHarp TCSPC module. The objects to be imaged were placed at 1.5 m to 2.5 m distance from the optical setup. The laser and the single-photon detector were placed in the same horizontal plane, at a separation of 7 cm, making our imaging setup effectively monostatic.

### Radiometric calibration:

The detection efficiency is the product of the interference filter's transmission and the detector's quantum efficiency,  $\gamma = 0.49 \times 0.35 = 0.17$ . A reference calibration for  $S$ , the average photon number in the backreflected signal received from single-pulse illumination of a near-unity reflectivity pixel, was obtained as follows. All sources of background light were turned off, and the laser was used to illuminate a transverse location  $(x_{\text{ref}}, y_{\text{ref}})$  on a highly-reflective Lambertian surface at a distance of 2 m. The average number of transmitted pulses before a photon detection was found to be  $\langle n(x_{\text{ref}}, y_{\text{ref}}) \rangle = 65$ . Using Eq. 1 from the paper, with  $\alpha(x_{\text{ref}}, y_{\text{ref}}) = 1$  and  $B = 0$ , we find

$$\langle n(x_{\text{ref}}, y_{\text{ref}}) \rangle = \frac{1}{1 - P_0(x_{\text{ref}}, y_{\text{ref}})} = \frac{1}{1 - \exp(-\gamma S)},$$

from which  $\langle n(x_{\text{ref}}, y_{\text{ref}}) \rangle = 65$  and  $\gamma = 0.17$  give  $S = 0.09$ .

For adjusting background illumination power, the laser was first turned off and all objects were removed from the scene. Then the incandescent lamp's optical power was adjusted such that the average number of background photons reaching the detector in a pulse repetition pe-

riod was  $BT_r = 0.1$ .

#### Capturing reference images and 3D forms:

Accurate data for calibration and comparison were acquired by reducing background illumination to a negligible level, followed by point-by-point acquisition using a large number of photon detections at each transverse location. High-quality reflectivity images were formed by measuring the number of detections within a fixed dwell time ( $\sim 10$  msec/pixel). Millimeter-accurate 3D data were captured using the photon-count histogram method with 1000 photon arrival times per pixel.

#### Transverse optical calibration:

A geometric calibration is necessary to relate the reconstructed data to the actual 3D scene points. This was accomplished by first capturing high-quality images (using the baseline methods described above) of three different views of a planar checkerboard. Then a standard computer vision package, OpenCV: Open Source Computer Vision Library, was used to compute the optical center coordinates, perspective projection matrix, and radial lens distortion coefficients. Also, at transverse location  $(x, y)$ , the estimate  $Z(x, y)$  is a measurement of the radial distance to the object from the optical center. For visualization with a 3D graphics package, we convert the estimate  $[x, y, Z(x, y)]$  to 3D Cartesian coordinates using a geometric transformation (29).

#### First-photon data acquisition:

To generate one complete data set, we raster scan over  $1000 \times 1000$  pixels with the two-axis galvo. For transverse location  $(x, y)$ , only two values are recorded:  $n(x, y)$ , the number of laser pulses transmitted prior to the first detection event; and  $t(x, y)$ , the timing of the detection relative to the pulse that immediately preceded it. (Because our entire scene was contained within a few meters of the imaging setup, our 100 ns pulse repetition period guaranteed that each non-background photon detection came from the immediately preceding laser pulse.) In this work, we use the same data set for the reference images and first-photon images. While the reference images are obtained by averaging over  $\sim 1000$  photon detections at every pixel, the first-photon imager reads only the first detection recorded at every pixel, ignoring the rest of the data in the file. If we did not need to acquire a reference image for comparison, it would be possible to acquire a megapixel first-photon scan in approximately 20 minutes using our current equipment. This time estimate is limited only by the mechanical speed of our two-axis galvo;

our photon flux is high enough to permit much faster acquisition.

#### Photon-flux waveform measurement:

For range estimation, our computational imager requires knowledge of the laser pulse's photon-flux waveform. We use  $s(t)$  to denote the normalized ( $\int s(t) dt = 1$ ) version of this waveform for a laser pulse emitted at  $t = 0$ . This pulse shape was measured by directly illuminating the detector with highly attenuated laser pulses and binning the photon arrival times to generate a histogram of photon counts. Fitting a skewed Gamma function to this histogram yielded

$$s(t) \propto (t - T_s)^4 \exp\left(-\frac{(t - T_s)}{T_c}\right), \quad (\text{S1})$$

where  $T_s = 80$  ps and  $T_c = 40$  ps (see Fig. S1). The RMS pulse duration is defined as

$$T_p = \sqrt{\int_0^{T_r} (t - \bar{T})^2 s(t) dt},$$

where

$$\bar{T} = \int_0^{T_r} t s(t) dt$$

and  $T_r$  is the pulse repetition period.

#### Computational reconstruction of reflectivity (Step 1):

Using Eq. 1 from the paper, the negative of the log-likelihood function relating the pulse count data,  $n(x, y)$ , to the reflectivity parameter,  $\alpha(x, y)$ , at each transverse location is

$$\mathcal{L}(\alpha(x, y) | n(x, y)) = \gamma[\alpha(x, y) S + B T_r] [n(x, y) - 1] - \log[\gamma(\alpha(x, y) S + B T_r)]$$

(see Supplementary Proofs for derivation). This is a strictly convex function of  $\alpha(x, y)$ .

Spatial correlations present in the object reflectivity are captured by wavelet-domain sparsity. For this work we used the discrete wavelet transform (DWT) derived from Daubechies's 4-tap filters (30). This transform  $\Phi(\cdot)$  is implemented as a matrix multiplication. With some abuse of notation, because  $\alpha(x, y)$  is also used for the true reflectivity, let the 2D reflectivity image be denoted by  $\{\alpha(x, y)\}_{x,y=1}^{1000}$ . Also let  $\{w(x, y)\} = \Phi(\{\alpha(x, y)\})$  denote the collection of DWT coefficients. A standard measure of sparsity used in image processing is the sum of absolute values of DWT coefficients, denoted here using the  $\ell_1$ -norm:

$$\|\Phi(\{\alpha(x, y)\})\|_1 = \sum_x \sum_y |w(x, y)|.$$

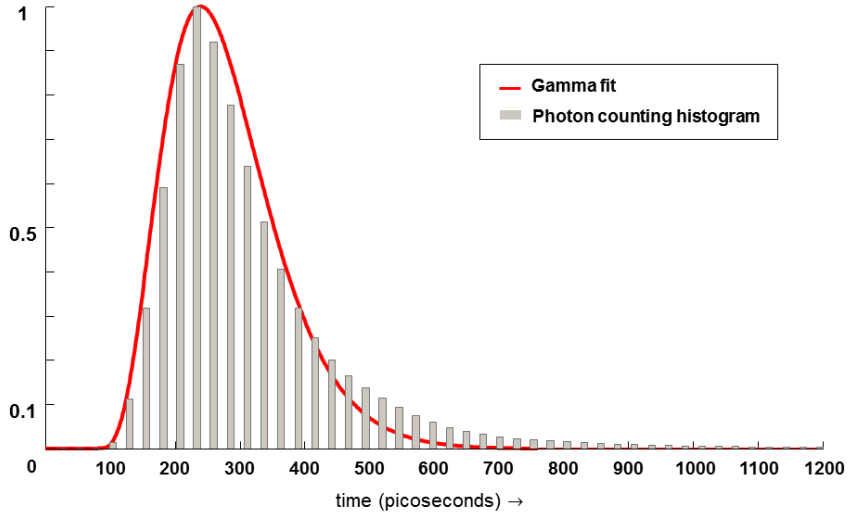


**Figure S1: Pulse shape measurement.** Plot of photon-count histogram overlaid with the fitted pulse shape. The histogram and the fitted pulse shape have been normalized to have unity maximum values.

It is well known that  $\|\Phi(\{\alpha(x, y)\})\|_1$  is a strictly convex function of the image  $\{\alpha(x, y)\}$  (17).

The reflectivity estimate is computed by minimizing—over the set of all possible images—the sum of negative log-likelihood functions over all transverse locations and the sparsity measuring function. A weight parameter,  $\beta \in [0, 1]$ , needs to be introduced to trade off between the likelihood and sparsity terms in the objective function. For a fixed  $\beta$ , the reflectivity estimation problem is the optimization program:

$$\begin{aligned} & \underset{\{\alpha(x, y)\}}{\text{minimize}} \quad (1 - \beta) \sum_x \sum_y \mathcal{L}(\alpha(x, y) | n(x, y)) + \beta \|\Phi(\{\alpha(x, y)\})\|_1 && \text{(OPT-1)} \\ & \text{subject to} \quad \alpha(x, y) \geq 0, \quad \text{for all } x, y. \end{aligned}$$

OPT-1 is a strictly convex optimization program, because it is the nonnegative weighted sum of individually convex functions. It is solved using standard numerical methods described in (18). The constraint  $\alpha(x, y) \geq 0$  captures the fact that reflectivity is nonnegative.

Each  $\beta$  value produces a candidate reflectivity image. We selected a  $\beta$  value by solving the optimization problem OPT-1 for  $\beta = \{0.1, 0.2, \dots, 0.9\}$  and then choosing the one that minimized the objective function defined in OPT-1.

### Background noise censoring (Step 2):

At each transverse location,  $(x, y)$ , the ROAD statistic is first computed using the time-of-arrival measurements of the eight nearest transverse neighbors, denoted by  $(x_1, y_1), \dots, (x_8, y_8)$ . Except at the boundaries, these neighbors are

$$(x-1, y-1), (x-1, y), (x-1, y+1), (x, y-1), (x, y+1), (x+1, y-1), (x+1, y), (x+1, y+1).$$

The eight absolute time-of-arrival differences

$$|t(x_1, y_1) - t(x, y)|, \dots, |t(x_8, y_8) - t(x, y)|$$

are sorted in ascending order, and the ROAD statistic  $\text{ROAD}(x, y)$  is the sum of the first four absolute differences from this sorted collection.

Then, a binary hypothesis test is applied to classify the photon detection at  $(x, y)$  as being due to background light. To apply this test, we require an accurate reflectivity estimate,  $\alpha(x, y)$ , which we obtained in Step 1. Using this reflectivity estimate, and the theory of merged Poisson processes (31), we obtain the following probabilities:

$$\Pr[\text{detected photon is due to background light}] = \frac{BT_r}{\alpha(x, y)S + BT_r},$$

$$\Pr[\text{detected photon is due to backreflected signal}] = \frac{\alpha(x, y)S}{\alpha(x, y)S + BT_r}.$$

These probabilities are used to generate thresholds used in the binary hypothesis test based on the computed ROAD statistic. The test is as follows:

<b>if</b> $\text{ROAD}(x, y) \geq 4T_p \frac{BT_r}{\alpha(x, y)S + BT_r}$ ,	<b>then</b> the detected photon is censored;
<b>if</b> $\text{ROAD}(x, y) < 4T_p \frac{BT_r}{\alpha(x, y)S + BT_r}$ ,	<b>then</b> the detected photon is <i>not</i> censored.

### Computational reconstruction of 3D structure (Step 3):

Using Eq. 2 from the paper and the fitted pulse shape (Eq. S1), the negative of the log-likelihood function relating the signal photon's arrival time,  $t(x, y)$ , to the distance,  $Z(x, y)$ , at each *uncensored* spatial location is

$$\begin{aligned} \mathcal{L}(Z(x, y) \mid t(x, y)) &= -\log \left[ s \left( t(x, y) - \frac{2Z(x, y)}{c} \right) \right] \\ &= -4 \log \left[ t(x, y) - T_s - \frac{2Z(x, y)}{c} \right] - \frac{t(x, y) - T_s - 2Z(x, y)/c}{T_c}, \end{aligned}$$

(see Supplementary Proofs for derivation). This negative log-likelihood is a strictly convex function of  $Z(x, y)$ .

As was done for reflectivity estimation in Step 1, spatial correlations present in the 3D form are captured by wavelet-domain sparsity. Again with some abuse of notation, because  $Z(x, y)$  is also used for the true range, let the 3D image be  $\{Z(x, y)\}_{x,y=1}^{1000}$ . The 3D estimate is computed by minimizing—over the set of all possible 3D forms—the sum of negative likelihood functions over the uncensored spatial locations and the sparsity measuring function. As before, a weight parameter,  $\beta \in [0, 1]$ , needs to be introduced. For a fixed  $\beta$ , the 3D reconstruction problem is the following optimization program:

$$\begin{aligned} & \underset{\{Z(x,y)\}}{\text{minimize}} \quad (1 - \beta) \sum_{\text{uncensored } (x,y)} \mathcal{L}(Z(x, y) \mid t(x, y)) + \beta \|\Phi(\{Z(x, y)\})\|_1 && \text{(OPT-2)} \\ & \text{subject to} \quad Z(x, y) \geq 0, \quad \text{for all } x, y. \end{aligned}$$

The constraint  $Z(x, y) \geq 0$  captures the fact that distance is always nonnegative. Note that  $\Phi(\{Z(x, y)\})$  is a function of the entire 3D image, i.e., range values are assigned to  $(x, y)$  locations whose arrival times were censored because they were predicted to originate from background light. We solved the optimization problem OPT-2 for  $\beta = \{0.1, 0.2, \dots, 0.9\}$ , and the final 3D estimate was the one whose  $\beta$  value minimizes the objective function in OPT-2.

#### Numerical details and image formation time:

The starting points for optimization problems OPT-1 and OPT-2 were the pointwise estimates,

$$\begin{aligned} \hat{\alpha}_{\text{ML}}(x, y) &= \max \left\{ \frac{1}{(n(x, y) - 1) \gamma S} - \frac{B T_r}{S}, 0 \right\} \\ \hat{Z}(x, y) &= \begin{cases} c(t(x, y) - T_m)/2, & \text{for uncensored spatial locations} \\ 0, & \text{for censored spatial locations,} \end{cases} \end{aligned}$$

where  $T_m = \arg \max s(t)$ . For solving the optimization problems we use the numerical methods based on SPIRAL-TAP (18). These methods are also the basis of our MATLAB implementation included with the zipped archive containing supplementary experimental data. For a 1 megapixel reflectivity and 3D reconstruction, the total run time required by the 9 instances of OPT-1 followed by ROAD filtering and 9 instances of OPT-2 was less than 3 minutes for all processed datasets. The convex optimization solver reached the desired precision and terminated after 4 or 5 iterations. The computation was carried out on a standard desktop computer with 4 GB memory and Intel Core 2 Duo processor (2.7 GHz).

## Supplementary Text

### Range resolution test:

To test range resolution, we created a resolution chart with  $5\text{ cm} \times 5\text{ cm}$  square plates mounted on a flat board to present our imager with targets of varying heights from that board (see Fig. S2). This test target was placed at a range of 3 m and first-photon data was acquired. The 3D form was then reconstructed using our computational imager. For comparison, the pointwise ML 3D estimate based on first-photon arrivals was computed, and the photon-count histogram method using 115 photons at each transverse location was also implemented. The reconstruction results are all shown in Fig. S3.

As discussed in detail in the next section, we use a histogram-based analysis to quantify our achievable range resolution. As shown in Fig. S4, our method achieves a range resolution slightly better than 4 mm using only first-photon detections. In contrast, the pointwise maximum-likelihood 3D estimates are extremely noisy, and the pointwise photon-count histogram method requires 115 photon detections at each transverse location to achieve  $\sim 4$  mm accuracy under identical imaging conditions.

Given a single (signal) photon arrival time, the RMS pulse duration of 226 ps corresponds to  $cT_p/2 = 34$  mm range uncertainty. At the background level in our experiment, the RMS error in the first-photon pointwise estimate is equal to  $(c/2)\sqrt{(T_p^2 + T_r^2/12)/2} = 3.06$  m (see Supplementary Proofs for derivation). In comparison, the 4 mm range resolution achieved by our computational imager is 8.5 times smaller than the RMS pulse duration and 765 times smaller than the RMS range error of the first-photon pointwise estimate.

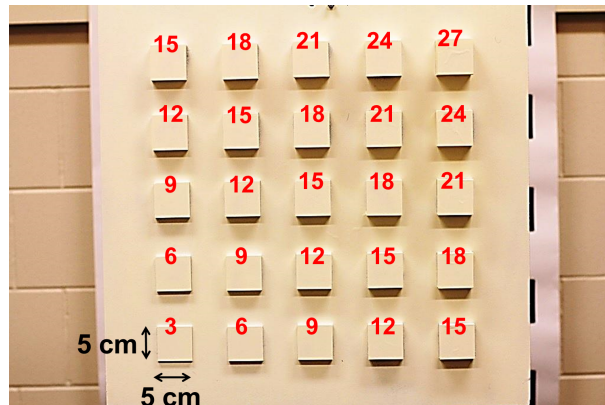


**Figure S2: Photograph of the range-resolution test target.** The height of the squares (in millimeters) relative to the flat surface is overlaid in red in this image. Each square has dimensions  $5\text{ cm} \times 5\text{ cm}$  (marked in black).

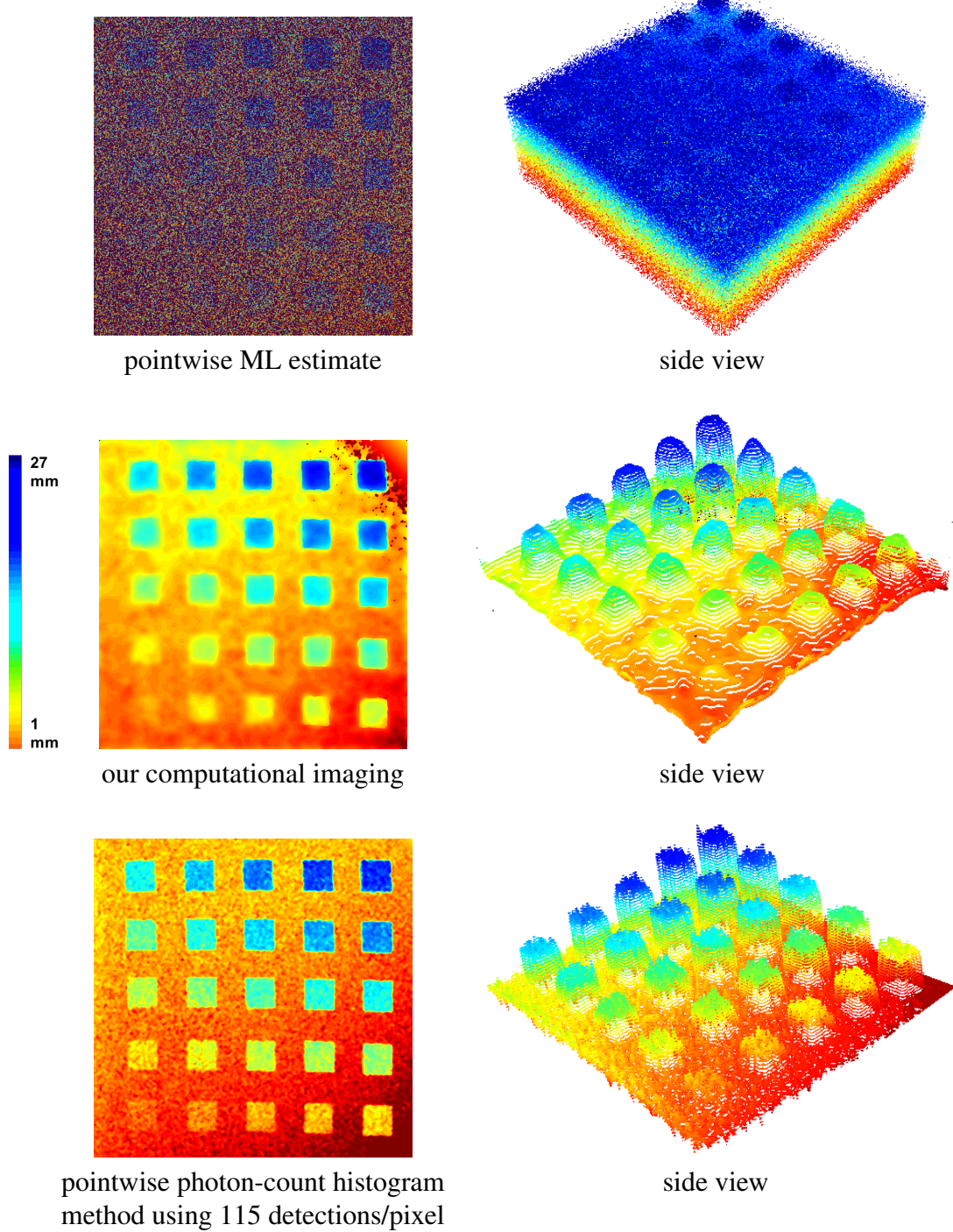


**Figure S3: Range resolution test.** The color bar indicates the height of the squares above the flat surface. The first-photon pointwise ML estimate is noisy. With our computational imager and the photon-count histogram method, the square in the bottom left (3 mm above the surface) is barely visible, but the other squares are clearly distinguishable. Histogram analysis in Fig. S4 indicates  $\sim 4$  mm range resolution of our computational imager.

### Statistical analysis of range resolution test:

We use a histogram-based analysis to quantify the achievable range resolution. We plot a histogram of the reconstructed depth values in the neighborhood of an edge of the square plates of different heights (see Figs. S4 and S5).

As demonstrated in Fig. S4, the depth histograms generated using the first-photon imaging have two clearly distinguishable components in the edge regions A and D: one corresponding to the points on the flat board and the other centered near the height of the square (6 mm). The variance or spread in these histograms is due to reconstruction errors as well as the inherent radial depth variations. The difference in the mean values of these two clearly distinguishable histogram components is approximately 4 mm, which also corresponds to the range resolution of our computational imager. As expected, the histogram components in edge region B are also well-separated. Finally, in the edge region C corresponding to a square plate of height 3 mm, it is not possible to resolve the different range components and identify a depth edge, demonstrating the resolution limit of our imager.

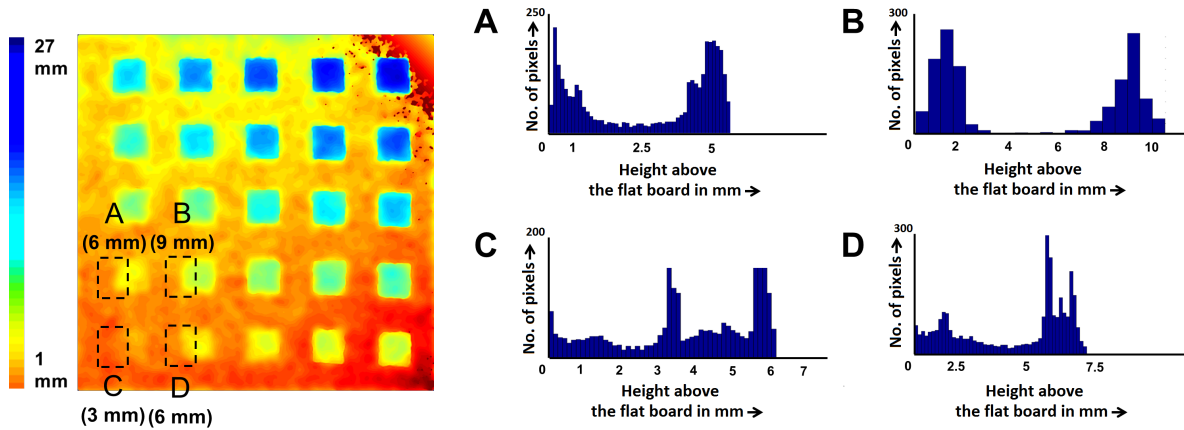


**Figure S4: Statistical analysis of range resolution test for first-photon imaging.** To quantify the achievable 4 mm range resolution of our computational imager we histogram the reconstructed pixel heights in the neighborhoods of depth edges (A-D). The height of a pixel is the difference of its reconstructed depth value and the depth of the bottom-left most corner of the flat board. The difference in the mean values of clearly separated histogram components in the edge regions A and D is 4 mm, which is also the range resolution of the first-photon imager.

Similar histogram analysis is conducted for the pointwise photon-counting histogram method which uses 115 photon detections/pixel (see Fig. S5). As demonstrated in Fig. S5, the histogram-based analysis yields depth resolution that is similar to that of first-photon imaging.

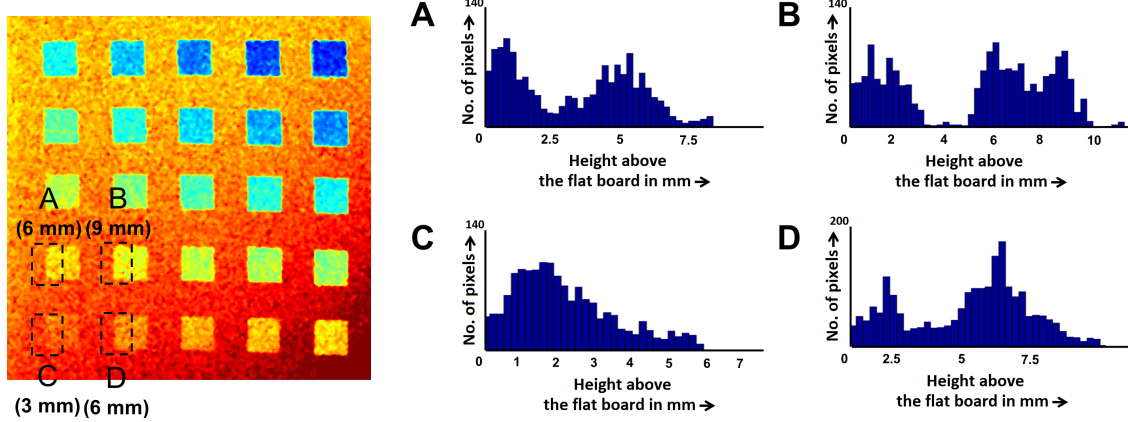


**Figure S5:** Statistical analysis of range resolution test for photon-counting histogram method using 115 photon detections/pixel.

**Reflectivity resolution test:** To test the reflectivity resolution achievable with our computational imager, we printed a linear gray-scale chart on matte paper. (see Fig. S6). This test target was placed at a range of 4 m and a reference image was acquired with a 1 msec dwell time at each pixel. We then used our computational imager to reconstruct the reflectivity using only the first photon detections at each pixel, ignoring the rest of the data. For comparison, pointwise maximum-likelihood estimates based on first-photon data were also computed.

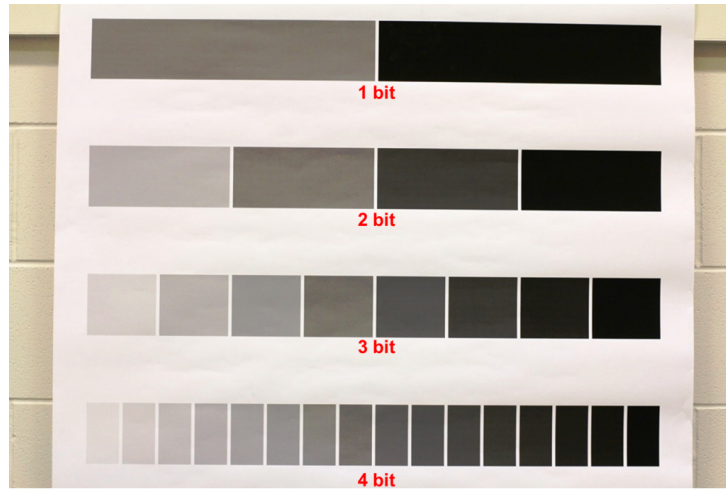


**Figure S6:** Photograph of the reflectivity-resolution test target.

The number of distinguishable gray levels is an indicator of the reflectivity resolution achieved by the imager. As shown in Fig. S7, our method is able to discriminate 16 gray levels, which implies a reflectivity resolution of at least 4 bits using only first-photon detections. In comparison, the pointwise maximum-likelihood estimation allows visual discrimination of about 3

gray levels. Our computational imager achieves a reflectivity resolution similar to that of the baseline measurement, which required at least 900 photon detections per pixel.

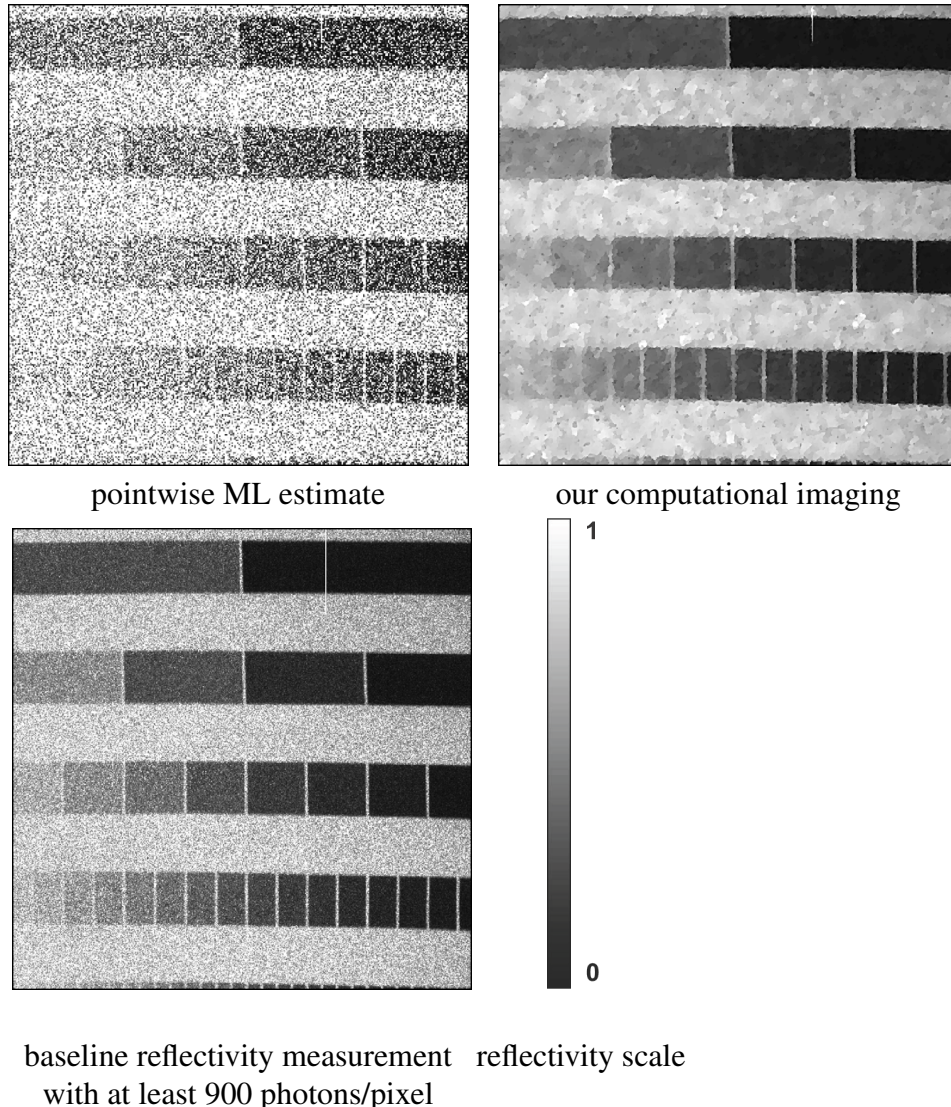


**Figure S7: Reflectivity resolution test.** The reflectivity scale is relative to that of the calibration point,  $\alpha(x_{\text{ref}}, y_{\text{ref}})$ , on a 0 to 1 scale.

#### Statistical analysis of reflectivity resolution test:

Similar to the histogram-based analysis of depth resolution, we plot the histogram of reconstructed reflectivity values in the image regions corresponding to linear gray-scales comprising different numbers of bits (highlighted in red) on the reflectivity test chart in Fig. S6. These

histograms and cumulative distribution plots are generated for each of the following methods: pointwise ML estimation, first-photon imaging, and the baseline reflectivity measurement requiring at least 900 detected photons/pixel.

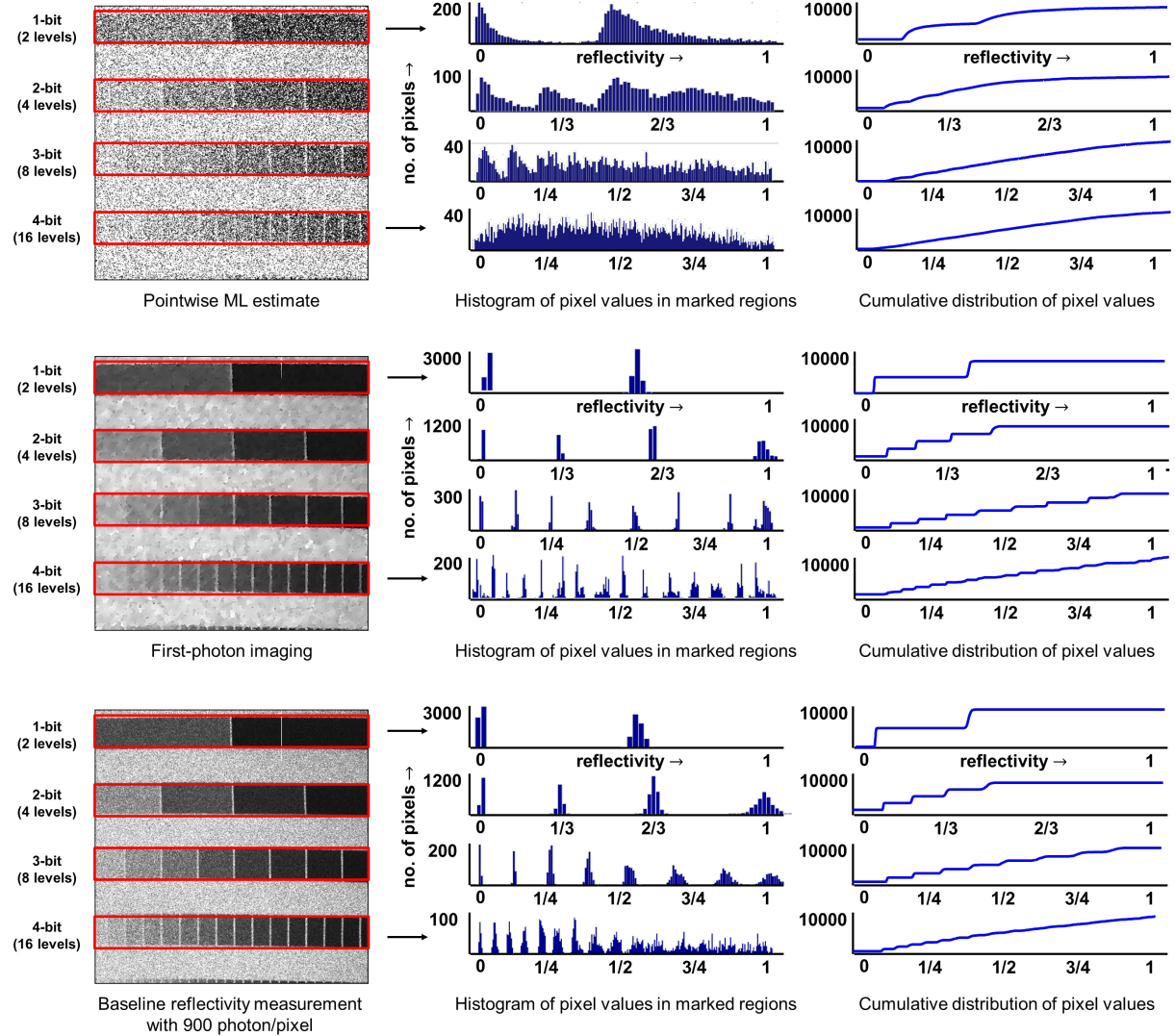
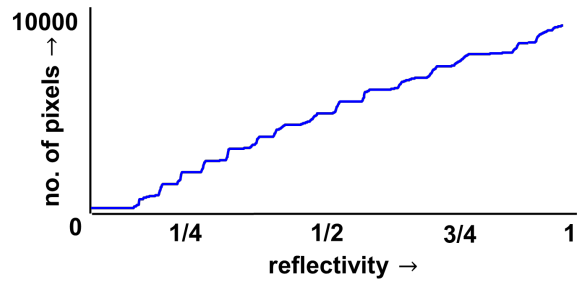


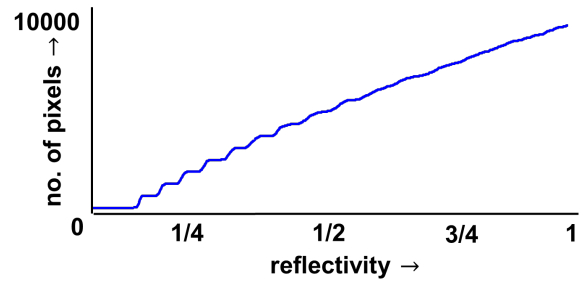
**Figure S8: Histogram-based analysis of reflectivity resolution.**

As demonstrated in Fig. S8, the pointwise ML estimation fails to clearly identify more than 3 gray levels, whereas first-photon imaging can distinguish 16 gray levels, each with low variance (also shown in Fig. S9).

The baseline reflectivity estimation method, which uses at least 900 detected photons/pixel,



First-photon imaging



Baseline reflectivity measurement  
with 900 photon/pixel

**Figure S9: Cumulative distribution plots showing 16 steps correponding to the reflectivity levels in Fig. S6.**

gives slightly worse performance than our method because of the high variance in the histogram components arising from Poisson noise. The use of spatial correlations in our technique mitigates this Poisson noise and results in clearly resolvable reflectivity levels.

Imaging of additional scenes:

Three additional scenes, consisting of real-world objects, were imaged. For each dataset, the pointwise maximum-likelihood estimate and the computationally reconstructed images are shown (Figs. S10–S12).

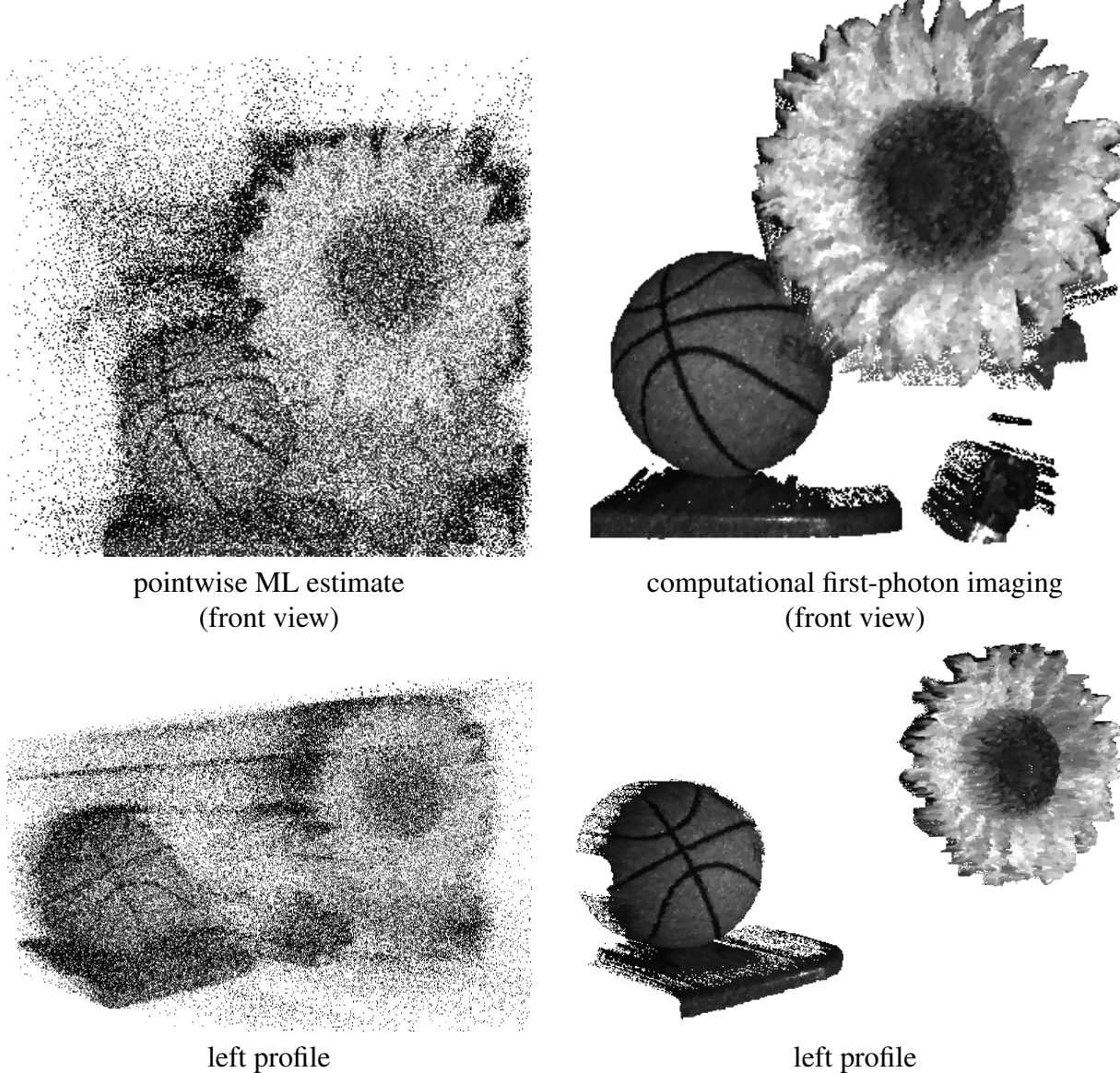
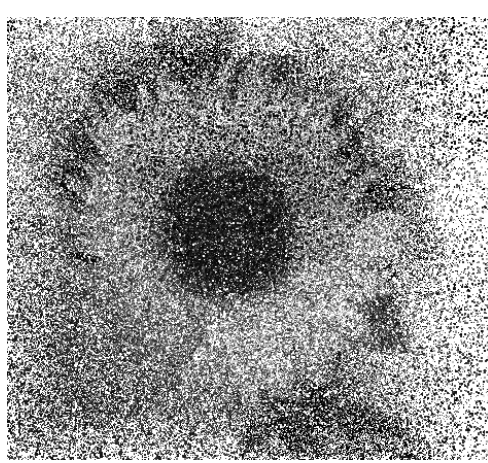


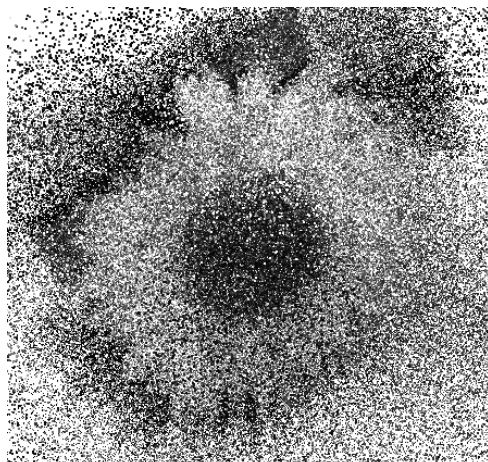
**Figure S10: Layered scene with two life-sized objects.**



pointwise ML estimate  
(front view)



computational first-photon imaging  
(front view)

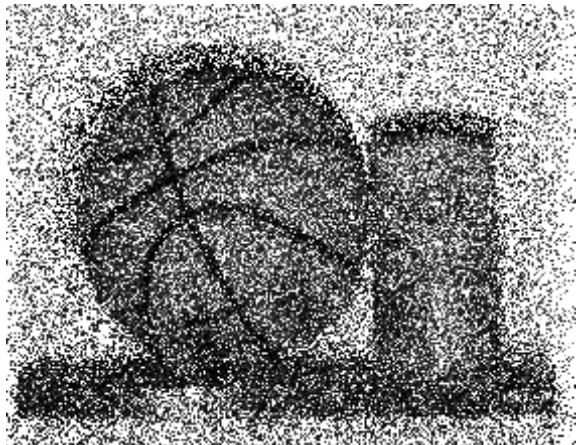


right profile



right profile

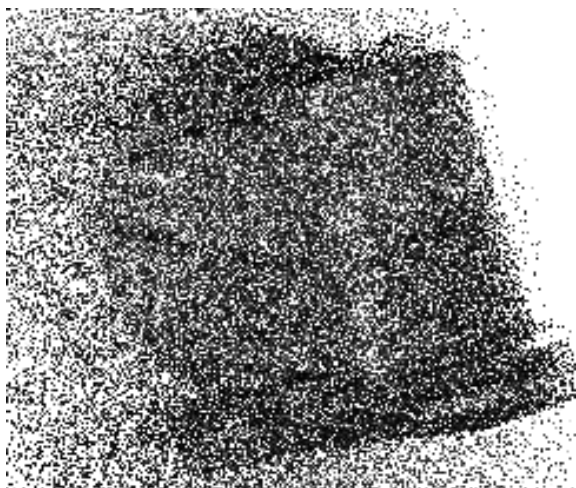
**Figure S11: Sunflower dataset reconstruction.** The lateral dimensions of the sunflower were approximately  $20\text{ cm} \times 20\text{ cm}$ . The depth variation of the petals and the flower center was approximately 7 cm. The reconstructed 3D form is rendered as a point cloud overlaid with recovered reflectivity estimates. Notice the flying pixels at object boundaries in the left profile.



pointwise ML estimate  
(front view)



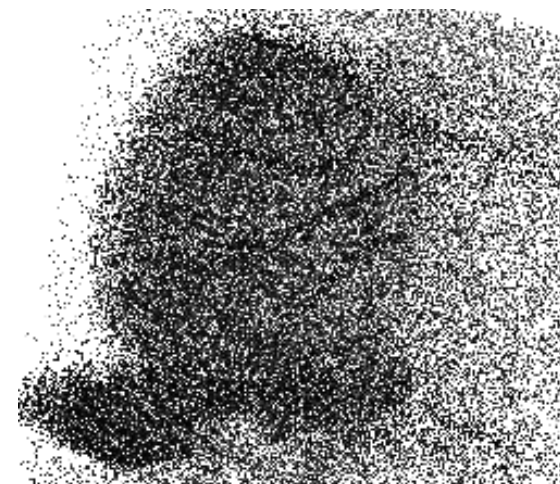
computational first-photon imaging  
(front view)



left profile



left profile



right profile



right profile

**Figure S12: Basketball and mug dataset reconstruction.** The basketball diameter was 40 cm.

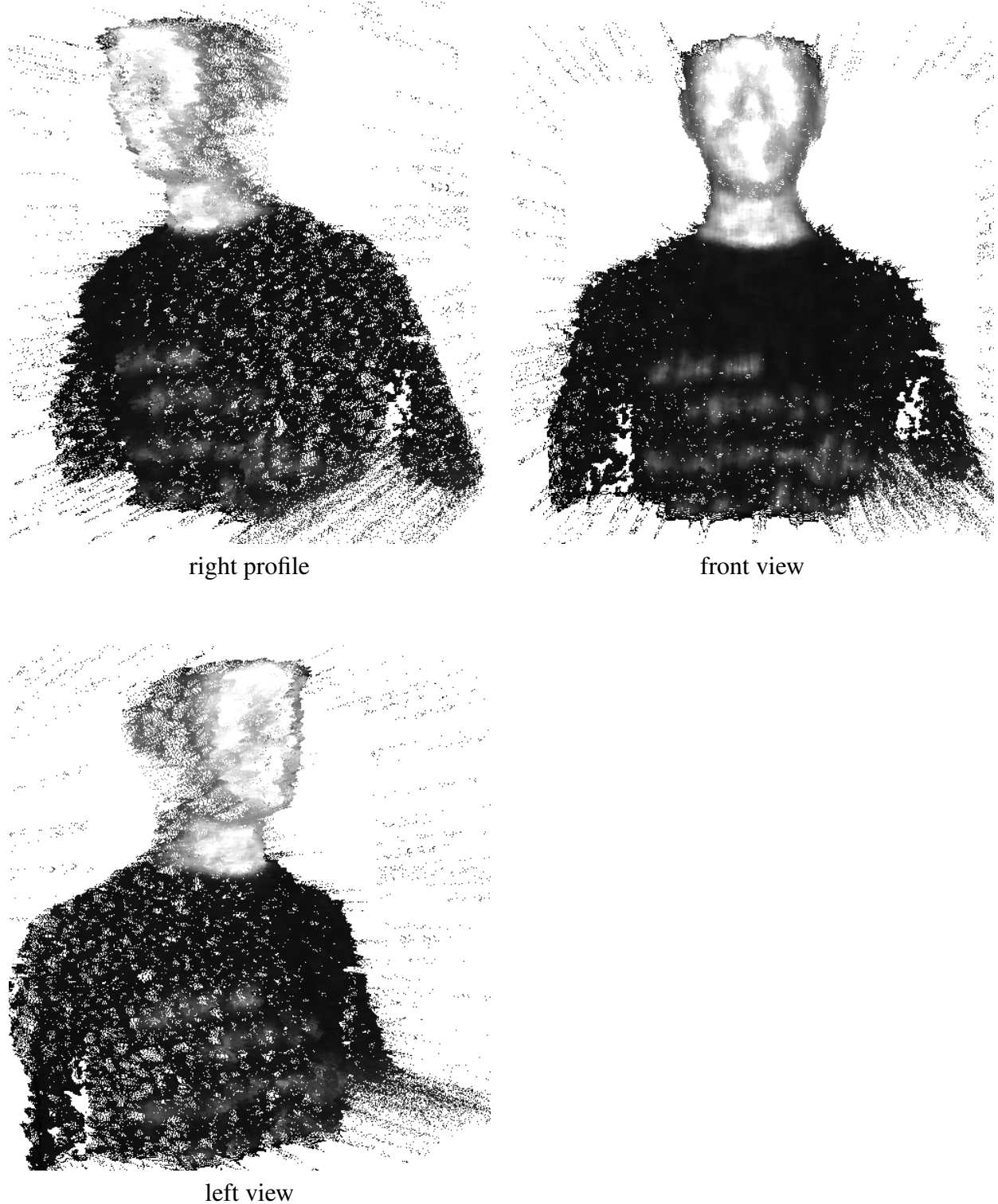


**Figure S13: Denoising first-photon data with median filtering.** The pointwise maximum-likelihood 3D and reflectivity estimates shown in Fig. 2(A)-(C) were separately median filtered. The smallest window size that mitigated noise was found to be  $9 \times 9$ . As shown in the different rendered profiles overlaid with reflectivity data, noise mitigation using median filtering significantly degrades spatial features.

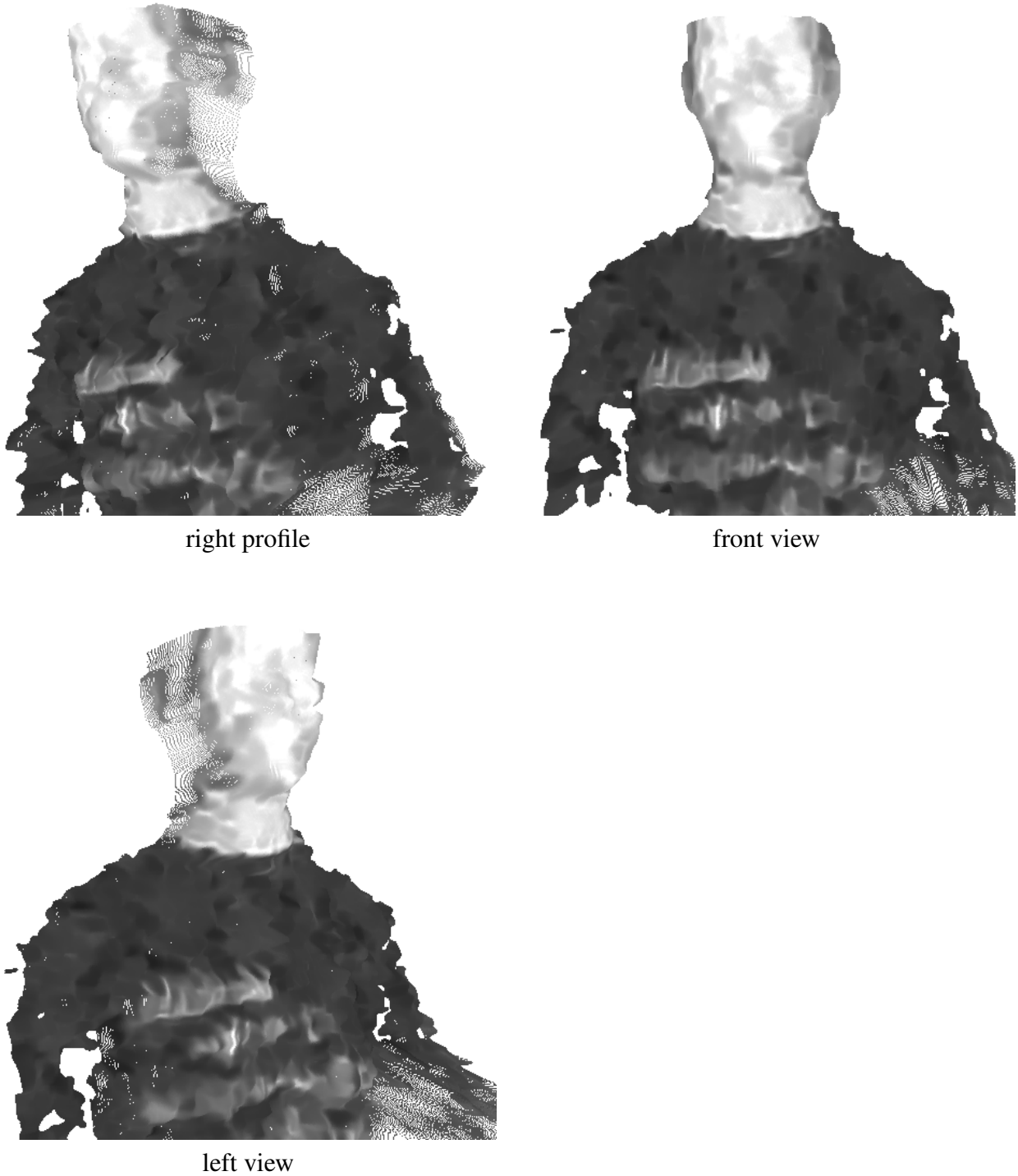


**Figure S14: Denoising first-photon data with BM3D.** The pointwise maximum-likelihood 3D and reflectivity estimates shown in Fig. 2(A)-(C) were separately filtered using the state-of-the-art BM3D algorithm. As shown in the different rendered profiles, noise mitigation using BM3D significantly degrades spatial features.

**Table S1: Mathematical notation used in the paper.**

<b>Notation</b>	<b>Description</b>
$(x, y)$	two-dimensional index for transverse location
$t(x, y)$	arrival time of first detected photon at transverse location $(x, y)$ , measured relative to the preceding illumination pulse (seconds)
$n(x, y)$	number of illumination pulses at transverse location $(x, y)$ prior to first photon detection
$\alpha(x, y)$	scene reflectivity at transverse location $(x, y)$ (nonnegative quantity, unitless)
$Z(x, y)$	object range at transverse location $(x, y)$ (meters)
$B$	photon arrival rate generated by background illumination (counts per second)
$S$	average number of laser photons arriving at the detector in response to a single-pulse illumination of a unity-reflectivity spatial location (photons)
$\gamma$	detection efficiency (unitless)
$T_r$	pulse repetition period (seconds)
$P_0(x, y)$	probability of not detecting a photon when transverse location $(x, y)$ is illuminated with a single laser pulse
$\hat{\alpha}_{\text{ML}}(x, y)$	pointwise maximum-likelihood reflectivity estimate using first-photon data
$\hat{Z}(x, y)$	pointwise 3D estimate based on first photon data
$c$	speed of light (meters per second)
$T_p$	root mean square (RMS) duration of laser pulse's photon-flux waveform (seconds)
$s(t)$	normalized (to unit area) photon-flux waveform of a laser pulse launched at $t = 0$ (1/seconds)

## Supplementary Proofs

Derivation of probability  $P_0(x, y)$ :

Consider first-photon detection while illuminating transverse location  $(x, y)$ . The optical flux incident on the single-photon detector is the sum of backreflected laser light from a single illumination pulse and background light. Thus the detector's average photon count in a  $T_r$ -sec pulse repetition period is  $\gamma(\alpha(x, y)S + BT_r)$ . Then, using Poisson photon-counting statistics, the probability mass function for the number of observed counts  $N$  is

$$\Pr[N = k] = \frac{e^{-\gamma(\alpha(x,y)S+BT_r)} (\gamma(\alpha(x,y)S+BT_r))^k}{k!}, \quad \text{for } k = 0, 1, 2, \dots.$$

The probability,  $P_0(x, y)$  of *not* detecting a photon in response to a single illumination pulse is

$$P_0(x, y) = \Pr[N = 0] = e^{-\gamma(\alpha(x,y)S+BT_r)}.$$

Pointwise maximum-likelihood reflectivity estimate:

At each transverse location, the maximum-likelihood estimate for that location's reflectivity,  $\alpha(x, y)$ , is obtained by finding the reflectivity value that maximizes the likelihood (Eq. 1 from the paper)—or, equivalently, the logarithm of the likelihood—given the pulse count data  $n(x, y)$ , i.e.,

$$\begin{aligned} \hat{\alpha}_{\text{ML}}(x, y) &= \arg \max_{\alpha: \alpha \geq 0} \log \left\{ e^{-\gamma(\alpha S + BT_r)[n(x,y)-1]} [1 - e^{-\gamma(\alpha S + BT_r)}] \right\} \\ &\approx \arg \max_{\alpha: \alpha \geq 0} \log \left\{ e^{-\gamma(\alpha S + BT_r)[n(x,y)-1]} [\gamma(\alpha S + BT_r)] \right\} \end{aligned} \quad (\text{S2})$$

$$\begin{aligned} &= \arg \max_{\alpha: \alpha \geq 0} -\gamma \alpha S [n(x, y) - 1] + \log(\alpha S + BT_r) \\ &= \arg \min_{\alpha: \alpha \geq 0} \gamma \alpha S [n(x, y) - 1] - \log(\alpha S + BT_r) \end{aligned} \quad (\text{S3})$$

Here (S2) uses the leading term in its Taylor series to approximate  $1 - e^{-\gamma(\alpha S + BT_r)}$ , which is valid because  $\gamma(S + BT_r) \ll 1$ . The objective function defined in (S3) will be shown below to be strictly convex. The solution to the optimization problem is the  $\alpha(x, y)$  value at which the objective function's derivative vanishes, unless that stationary-point value is negative. In the latter eventuality we set  $\hat{\alpha}_{\text{ML}} = 0$ , because of the nonnegativity constraint. This computation yields

$$\hat{\alpha}_{\text{ML}}(x, y) = \max \left\{ \frac{1}{(n(x, y) - 1) \gamma S} - \frac{BT_r}{S}, 0 \right\}.$$

Derivation of range-estimation error:

The pointwise 3D estimate is  $\hat{Z}(x, y) = c(t(x, y) - T_m)/2$ , where  $T_m$  is the mode of the normalized pulse shape  $\tilde{s}(t)$ . In our experiments, each photon detection is either due to backreflected laser light (the signal) or to background light. The conditional probability density functions for the first-photon's arrival time,  $t(x, y)$ , are

$$\begin{aligned} p_{t(x,y)|\text{signal}}(\tau) &= s(\tau - 2Z(x, y)/c), \quad \text{for } 0 \leq \tau < T_r, \\ p_{t(x,y)|\text{background}}(\tau) &= 1/T_r, \quad \text{for } 0 \leq \tau < T_r \end{aligned}$$

(see below for derivations). The variance of the pointwise estimate  $\hat{Z}(x, y)$  is at least as large as the conditional variance of  $\hat{Z}(x, y)$  given knowledge of whether a detected photon is due to signal or background. Using the distribution of  $t(x, y)$  for detection of signal photons, we get

$$\text{var}(\hat{Z}(x, y) \mid \text{signal}) = \frac{c^2}{4} \text{var}(t(x, y)) = \frac{c^2 T_p^2}{4},$$

where we have used  $T_p \ll T_r$ . Using the distribution of  $t(x, y)$  for detection of background photons, we get

$$\text{var}(\hat{Z}(x, y) \mid \text{background}) = \frac{1}{12} \left( \frac{cT_r}{2} \right)^2.$$

Because detections that are due to signal and background occur with approximately equal probability, the unconditional variance of  $\hat{Z}(x, y)$  is

$$\frac{1}{2} \frac{c^2 T_p^2}{4} + \frac{1}{2} \frac{c^2 T_r^2}{48}.$$

Taking the square root gives the unconditional standard deviation, which is the RMS error of pointwise range estimation:

$$\frac{c}{2} \sqrt{\frac{1}{2} \left( T_p^2 + \frac{T_r^2}{12} \right)}.$$

Derivation of signal photon time-of-arrival probability density function,  $p_{t(x,y)|\text{signal}}$ :

Suppose that the laser pulse emitted at  $t = 0$  interrogates spatial location  $(x, y)$  and that the resulting backreflected laser light leads to a first-photon detection in the interval  $0 \leq t < T_r$ .

Consider an incremental time interval of duration  $\delta t$  starting at time  $\tau \in [0, T_r)$ . Using time-inhomogeneous Poisson photon-counting statistics, we obtain the following probability:

$$\begin{aligned} & \Pr[\text{first photon was detected at } t \in [\tau, \tau + \delta) \text{ and was due to signal}] \\ &= \Pr[\text{no photons detected in } t \in [0, \tau)] \times \Pr[\text{signal photon detected in } t \in [\tau, \tau + \delta t)] \\ &\quad \times \Pr[\text{no background photon detected in } t \in [\tau, \tau + \delta t)] \\ &= \gamma \left[ \int_{\tau}^{\tau+\delta t} \alpha(x, y)s(t - 2Z(x, y)/c)S dt \right] \exp \left[ -\gamma \int_0^{\tau+\delta t} (\alpha(x, y)s(t - 2Z(x, y)/c)S + B) dt \right], \end{aligned}$$

where we used the fact that Poisson processes have at most one count in an incremental time interval. Defining

$$f(\tau) = \lim_{\delta t \rightarrow 0} \frac{\Pr[\text{first photon was detected at } t \in [\tau, \tau + \delta) \text{ and was due to signal}]}{\delta t},$$

the desired conditional probability density then follows from

$$\begin{aligned} p_{t(x,y)|\text{signal}}(\tau) &= \frac{f(\tau)}{\int_0^{T_r} f(\tau) d\tau} \\ &= \frac{s(\tau - 2Z(x, y)/c) \exp \left[ -\gamma \int_0^{\tau} (\alpha(x, y)s(t - 2Z(x, y)/c)S + B) dt \right]}{\int_0^{T_r} s(\tau - 2Z(x, y)/c) \exp \left[ -\gamma \int_0^{\tau} (\alpha(x, y)s(t - 2Z(x, y)/c)S + B) dt \right] d\tau} \\ &\approx s(\tau - 2Z(x, y)/c), \quad \text{for } 0 \leq \tau < T_r, \end{aligned}$$

where the approximation is valid under the low-flux condition,  $\gamma(S + BT_r) \ll 1$ . Our computational imager's censoring process (Step 2) is sufficiently good that it is safe to process uncensored arrival times as though they were due to signal-photon detections.

Derivation of background photon time-of-arrival probability density function,  $p_{t(x,y)|\text{background}}$ :

Suppose that the laser pulse emitted at  $t = 0$  interrogates spatial location  $(x, y)$  but background light is responsible for the first-photon detection in the interval  $0 \leq t < T_r$ . Consider an incremental time interval of duration  $\delta t$  starting at time  $\tau \in [0, T_r)$ . Using time-inhomogeneous Poisson photon-counting statistics, we obtain the following probability:

$$\begin{aligned} & \Pr[\text{first photon was detected at } t \in [\tau, \tau + \delta) \text{ and was due to background}] \\ &= \Pr[\text{no photons detected in } t \in [0, \tau)] \times \Pr[\text{background photon detected in } t \in [\tau, \tau + \delta t)] \\ &\quad \times \Pr[\text{no signal photon detected in } t \in [\tau, \tau + \delta t]] \\ &= \gamma B \delta t \exp \left[ -\gamma \int_0^{\tau+\delta t} (\alpha(x, y)s(t - 2Z(x, y)/c)S + B) dt \right], \end{aligned}$$

where we used the fact that Poisson processes have at most one count in an incremental time interval. Defining

$$g(\tau) = \lim_{\delta t \rightarrow 0} \frac{\Pr[\text{first photon was detected at } t \in [\tau, \tau + \delta) \text{ and was due to background}]}{\delta t},$$

the desired conditional probability density then follows from

$$\begin{aligned} p_{t(x,y)|\text{background}}(\tau) &= \frac{g(\tau)}{\int_0^{T_r} g(\tau) d\tau} \\ &= \frac{\exp[-\gamma \int_0^\tau (\alpha(x, y)s(t - 2Z(x, y)/c)S + B) dt]}{\int_0^{T_r} \exp[-\gamma \int_0^\tau (\alpha(x, y)s(t - 2Z(x, y)/c)S + B) dt] d\tau} \\ &\approx \frac{1}{T_r}, \quad \text{for } 0 \leq \tau < T_r, \end{aligned}$$

where the approximation is valid under the low-flux condition,  $\gamma(S + BT_r) \ll 1$ .

Proof of strict convexity of negative log-likelihoods:

The negative log-likelihood function for reflectivity estimation,  $\mathcal{L}(\alpha(x, y) \mid n(x, y))$ , is the objective function in Eq. S3:

$$\mathcal{L}(\alpha(x, y) \mid n(x, y)) = \gamma[\alpha(x, y)S + BT_r][n(x, y) - 1] - \log[\gamma(\alpha(x, y)S + BT_r)]$$

The second derivative of  $\mathcal{L}(\alpha(x, y) \mid n(x, y))$  with respect to the reflectivity  $\alpha(x, y)$  is  $S^2/(\alpha(x, y)S + BT_r)^2 > 0$ , confirming the strict convexity of  $\mathcal{L}(\alpha(x, y) \mid n(x, y))$  with respect to reflectivity.

The negative log-likelihood function for range estimation,  $\mathcal{L}(Z(x, y) \mid t(x, y))$ , is derived using Eq. 2 from the paper and Eq. S1:

$$\begin{aligned} \mathcal{L}(Z(x, y) \mid t(x, y) = \tau) &= -\log p_{t(x,y)|\text{signal}}(\tau) \\ &= -\log s(\tau - 2Z(x, y)/c) \\ &= \frac{(\tau - T_s - 2Z(x, y)/c)}{T_c} - 4 \log(\tau - T_s - 2Z(x, y)/c). \end{aligned}$$

The second derivative of  $\mathcal{L}(Z(x, y) \mid t(x, y) = \tau)$  with respect to the 3D parameter  $Z(x, y)$  is  $4/(\tau - T_s - 2Z(x, y)/c)^2 > 0$ , for all values of  $Z(x, y)$ . This fact confirms the strict convexity of  $\mathcal{L}(Z(x, y) \mid n(x, y))$  with respect to range.

## **Movie S1**

Movie S1 provides a visualization of the three steps involved in the computational reconstruction of reflectivity and 3D forms using first-photon data. It also provides a visualization of first-photon imaging reconstructions for three other datasets (sunflower, basketball and mug, and layered scene).

## **Movie S2**

Movie S2 is a demonstration of the repeatability of our computational method. It shows the data and the computational reconstruction of reflectivity and 3D estimates (visualized as range maps) for 500 independent first-photon data sets. At each pixel, the standard deviation of the 500 3D estimates is computed and visualized as an image, confirming the 4 mm range resolution achieved by the first-photon imager.

## References and Notes

1. J. C. Nicolas, Applications of low-light imaging to life sciences. *J. Biolumin. Chemilumin.* **9**, 139–144 (1994). [Medline doi:10.1002/bio.1170090307](#)
2. W. Becker, A. Bergmann, M. A. Hink, K. König, K. Benndorf, C. Biskup, Fluorescence lifetime imaging by time-correlated single-photon counting. *Microsc. Res. Tech.* **63**, 58–66 (2004). [Medline doi:10.1002/jemt.10421](#)
3. A. McCarthy, N. J. Krichel, N. R. Gemmell, X. Ren, M. G. Tanner, S. N. Dorenbos, V. Zwiller, R. H. Hadfield, G. S. Buller, Kilometer-range, high resolution depth imaging via 1560 nm wavelength single-photon detection. *Opt. Express* **21**, 8904–8915 (2013). [Medline doi:10.1364/OE.21.008904](#)
4. N. Savage, Single photon counting. *Nat. Photonics* **3**, 738–739 (2009). [doi:10.1038/nphoton.2009.232](#)
5. G. S. Buller, A. M. Wallace, Ranging and three-dimensional imaging using time-correlated single-photon counting and point-by-point acquisition. *IEEE J. Sel. Top. Quantum Electron.* **13**, 1006–1015 (2007). [doi:10.1109/JSTQE.2007.902850](#)
6. M. Jack, J. Wehner, J. Edwards, G. Chapman, D. N. B. Hall, S. M. Jacobson, HgCdTe APD-based linear-mode photon counting components and LADAR receivers. *Proc. SPIE* **8033**, 80330M (2011). [doi:10.1117/12.888134](#)
7. B. Schwarz, Mapping the world in 3D. *Nat. Photonics* **4**, 429–430 (2010). [doi:10.1038/nphoton.2010.148](#)
8. Y. Chen, J. D. Müller, P. T. C. So, E. Gratton, The photon counting histogram in fluorescence fluctuation spectroscopy. *Biophys. J.* **77**, 553–567 (1999). [Medline doi:10.1016/S0006-3495\(99\)76912-2](#)
9. S. Pellegrini, G. S. Buller, J. M. Smith, A. M. Wallace, S. Cova, Laser-based distance measurement using picosecond resolution time-correlated single-photon counting. *Meas. Sci. Technol.* **11**, 712–716 (2000). [doi:10.1088/0957-0233/11/6/314](#)
10. A. McCarthy, X. Ren, A. Della Frera, N. R. Gemmell, N. J. Krichel, C. Scarella, A. Ruggeri, A. Tosi, G. S. Buller, Kilometer-range depth imaging at 1,550 nm wavelength using an InGaAs/InP single-photon avalanche diode detector. *Opt. Express* **21**, 22098–22113 (2013). [Medline doi:10.1364/OE.21.022098](#)
11. D. L. Snyder, *Random Point Processes* (Wiley, New York, 1975).
12. M. E. O'Brien, D. G. Fouche, Simulation of 3D laser radar systems. *Lincoln Lab. J.* **15**, 37 (2005).
13. S. Geman, D. Geman, Stochastic relaxation, gibbs distributions, and the bayesian restoration of images. *IEEE Trans. Pattern Anal. Mach. Intell.* **PAMI-6**, 721–741 (1984). [Medline doi:10.1109/TPAMI.1984.4767596](#)
14. B. A. Olshausen, D. J. Field, Natural image statistics and efficient coding. *Netw. Comput. Neural Syst.* **7**, 333–339 (1996). [Medline doi:10.1088/0954-898X/7/2/014](#)

15. A. Srivastava, A. B. Lee, E. P. Simoncelli, S.-C. Zhu, On advances in statistical modeling of natural images. *J. Math. Imaging Vis.* **18**, 17–33 (2003).  
[doi:10.1023/A:1021889010444](https://doi.org/10.1023/A:1021889010444)
16. Supplementary materials are available on *Science Online*.
17. S. P. Boyd, L. Vandenberghe, *Convex Optimization* (Cambridge Univ. Press, Cambridge, 2004).
18. Z. T. Harmany, R. F. Marcia, R. M. Willett, This is SPIRAL-TAP: Sparse Poisson Intensity Reconstruction ALgorithms—theory and practice. *IEEE Trans. Image Process.* **21**, 1084–1096 (2012). [Medline](#) [doi:10.1109/TIP.2011.2168410](https://doi.org/10.1109/TIP.2011.2168410)
19. R. Garnett, T. Huegerich, C. Chui, W. He, A universal noise removal algorithm with an impulse detector. *IEEE Trans. Image Process.* **14**, 1747–1754 (2005). [Medline](#) [doi:10.1109/TIP.2005.857261](https://doi.org/10.1109/TIP.2005.857261)
20. A. M. Wallace, G. S. Buller, A. C. Walker, 3D imaging and ranging by time-correlated single photon counting. *Comput. Control Eng. J.* **12**, 157–168 (2001).  
[doi:10.1049/cce:20010403](https://doi.org/10.1049/cce:20010403)
21. K. Dabov, A. Foi, V. Katkovnik, K. Egiazarian, Image denoising by sparse 3-D transform-domain collaborative filtering. *IEEE Trans. Image Process.* **16**, 2080–2095 (2007). [Medline](#) [doi:10.1109/TIP.2007.901238](https://doi.org/10.1109/TIP.2007.901238)
22. W. Jiang, M. L. Baker, Q. Wu, C. Bajaj, W. Chiu, Applications of a bilateral denoising filter in biological electron microscopy. *J. Struct. Biol.* **144**, 114–122 (2003). [Medline](#) [doi:10.1016/j.jsb.2003.09.028](https://doi.org/10.1016/j.jsb.2003.09.028)
23. C.-W. Chang, M.-A. Mycek, Increasing precision of lifetime determination in fluorescence lifetime imaging. *Proc. SPIE* **7570**, 757007 (2010).  
[doi:10.1117/12.845787](https://doi.org/10.1117/12.845787)
24. S. Hernández-Marín, A. M. Wallace, G. J. Gibson, Bayesian analysis of Lidar signals with multiple returns. *IEEE Trans. Pattern Anal. Mach. Intell.* **29**, 2170–2180 (2007). [Medline](#) [doi:10.1109/TPAMI.2007.1122](https://doi.org/10.1109/TPAMI.2007.1122)
25. M. A. Albota, R. M. Heinrichs, D. G. Kocher, D. G. Fouche, B. E. Player, M. E. O'Brien, B. F. Aull, J. J. Zaykowski, J. Mooney, B. C. Willard, R. R. Carlson, Three-dimensional imaging laser radars with a photon-counting avalanche photodiode array and microchip laser. *Appl. Opt.* **41**, 7671–7678 (2002). [Medline](#) [doi:10.1364/AO.41.007671](https://doi.org/10.1364/AO.41.007671)
26. J. Busck, H. Heiselberg, Gated viewing and high-accuracy three-dimensional laser radar. *Appl. Opt.* **43**, 4705–4710 (2004). [Medline](#) [doi:10.1364/AO.43.004705](https://doi.org/10.1364/AO.43.004705)
27. G. N. Gol'tsman, O. Okunev, G. Chulkova, A. Lipatov, A. Semenov, K. Smirnov, B. Voronov, A. Dzardanov, C. Williams, R. Sobolewski, Picosecond superconducting single-photon optical detector. *Appl. Phys. Lett.* **79**, 705 (2001).  
[doi:10.1063/1.1388868](https://doi.org/10.1063/1.1388868)
28. S. Chen, D. Liu, W. Zhang, L. You, Y. He, W. Zhang, X. Yang, G. Wu, M. Ren, H. Zeng, Z. Wang, X. Xie, M. Jiang, Time-of-flight laser ranging and imaging at

- 1550 nm using low-jitter superconducting nanowire single-photon detection system. *Appl. Opt.* **52**, 3241–3245 (2013). [Medline doi:10.1364/AO.52.003241](#)
- 29. M. Lindner, A. Kolb, Lateral and depth calibration of pmd-distance sensors, in *Advances in Visual Computing*, G. Bebis *et al.*, Eds. (Springer, Berlin, 2006).
  - 30. S. G. Mallat, *A Wavelet Tour of Signal Processing* (Elsevier, Amsterdam, 2009).
  - 31. D. P. Bertsekas, J. N. Tsitsiklis, *Introduction to Probability* (Athena Scientific, Belmont, 2002).